INTERNATIONAL JOURNAL OF HYDROGEN ENERGY 44 (2019) 6245–6256

Available online at www.sciencedirect.com

ScienceDirect

journal homepage: www.elsevier.com/locate/he

Impact of ionomer resistance in nanofiber-nanoparticle electrodes for ultra-low platinum fuel cells

Monica Hwang, Yossef A. Elabd *

Department of Chemical Engineering, Texas A&M University, College Station, TX, 77843, United States

ARTICLE INFO

Article history:
Received 24 September 2018
Received in revised form
18 December 2018
Accepted 13 January 2019
Available online 7 February 2019

Keywords:
Nafion
Nanofiber
Electrospinning
Fuel cell
Platinum
Electrode

ABSTRACT

Previously, nanofiber-nanoparticle electrodes produced *via* a simultaneous electrospinning and electrospraying (E/E) process (E/E electrodes) resulted in polymer electrolyte membrane fuel cells with high power densities at ultra-low platinum (Pt) loadings (<0.1 mg_{Pt} cm^{-2}). In this study, E/E electrodes were fabricated at various Nafion contents to investigate the impact of ionomer content on catalyst layer transport resistances and fuel cell power density at ultra-low Pt loadings. Regardless of the Nafion content in the electrospray, the Nafion nanofiber diameters and catalyst aggregate particle sizes are constant in the E/E electrodes evidenced by electron microscopy. Therefore, this study allows for the exclusive investigation of the effect of transport resistances on fuel cell performances at different ionomer contents at a constant catalyst layer morphology, which differs from conventional electrodes. At higher magnifications, changes are evident in the micrographs around the catalyst aggregate particles, where an increase in ionomer thin film thickness is observed with increasing ionomer content. The maximum fuel cell performance and a minimum in catalyst layer resistance for E/E electrodes is observed at a total Nafion content of 62 wt%, which differs from conventional electrodes (*ca.* 30 wt%).

Introduction

Proton exchange membrane fuel cells (PEMFCs) are attractive alternative energy sources for large market applications, such as transportation, due to their high energy and power density, low-to-moderate temperature operation, use of fuels from renewable sources, and zero point-of-use carbon emissions. However, lowering fuel cell cost, while maintaining high power density, remains a global technological challenge that requires further research in the underlying transport mechanisms that transpire within the fuel cell [1,2]. Platinum (Pt), an expensive metal catalyst, significantly contributes to the fuel cell cost and is required due to the inherently slow oxygen reduction reaction (ORR) in the fuel cell acidic environment [3]. Numerous studies have investigated different aspects of the PEMFC (*e.g.*, novel catalysts [4,5], various operating conditions [6–8], alternative membranes [9–11]) to improve fuel cell power density at lower Pt loadings (<0.1 mg_{Pt} cm^{-2}; typical Pt loadings ~0.4–0.5 mg_{Pt} cm^{-2}) in order to reduce overall fuel cell cost. However, at lower Pt loadings, typically, there is a significant loss in fuel cell power density due the negative impact on the ORR in the electrode or catalyst layer (*i.e.*, increase in charge and mass transport resistances).

* *Corresponding author.*
E-mail address: elabd@tamu.edu (Y.A. Elabd).
https://doi.org/10.1016/j.ijhydene.2019.01.083

ORR within the fuel cell electrode can only occur at triple phase boundaries (pore-catalyst-ionomer interfaces or junctions) [12], where not only a higher number of these junctions are needed, but also a connected network of all three are also required, *i.e.*, pore network for O_2 transport, catalyst (Pt) network for electron transport, and ionomer (Nafion) network for proton transport [13]. Increasing the number and connectivity of triple phase boundaries can have a positive impact on the ORR by reducing both charge and mass transport resistances. Typically, the conventional electrode fabrication technique involves depositing a well-dispersed catalyst slurry solution (Nafion ionomer, Pt/C catalyst, and aqueous alcohol solvent) onto a substrate, typically a gas diffusion layer. After the solvent evaporates, the catalyst particles and ionomer create an intricate porous network, known as the catalyst layer, and allows physical contact between catalyst, ionomer, and pores to form multiple triple phase boundaries.

The impact of the porous catalyst layer structure on fuel cell performance has been extensively studied with the use of simulation models [14–18], different carbon materials [19–21], and various solvent compositions [22–25]. Specifically, studies on the effect of the ionomer content in the catalyst layer show that the ionomer content has a simultaneous impact on both the ionomer and pore network [26–32]. Passalacqua et al. [27] demonstrated that at low ionomer content, there is a loss of ionomer connectivity and subsequently proton conductivity or transport (*i.e.*, increases charge resistance), which lowers fuel cell performance. At higher ionomer contents, Uchida et al. [29] showed that pore volume decreases and blocks O_2 gas from reaching Pt reaction sites (*i.e.*, increases mass transfer resistance), which also lowers fuel cell performance. This finding was later supported by Lee et al. [30], who introduced the concept of the ionomer thin film resistance and reported that at higher ionomer contents, the ionomer thin film thickness increases and prevents O_2 from accessing Pt sites. Therefore, as illustrated in Fig. 1, there is a balance between ionomer connectivity and ionomer thin film resistance that limits the maximum power density due to the trade off in resistances in charge transfer (Fig. 1(a)) and mass transfer (Fig. 1(b)), respectively.

A number of studies have now investigated the role of the Nafion ionomer thin film and its impact on transport resistance and fuel cell performance with both *in situ* and *ex situ* investigations [14,33–46]. However, few studies provide insight on the role of transport resistances on fuel cell performance at low Pt loadings [47,48]. Greszler et al. [48] investigated the influence of Pt loading on oxygen transport resistance using limiting current density experiments and observed that fuel cell performance loss was significant at low Pt loadings. Owejan et al. [47] reported that fuel cells with ultra-low Pt loadings ($\leq$0.05 mg_{Pt} cm^{-2}) experienced significant transport losses and subsequently fuel cell performance losses and demonstrated that transport resistance is a strong function of the surface area and dispersion of particles (catalyst layer morphology). Both studies employed carbon as a filler to maintain similar porous catalyst layer morphologies and electrode thicknesses under different Pt loadings in order to investigate the ionomer thin film resistance. However, in these studies, the overall distribution of Pt catalyst differed due to the additional carbon (*i.e.*, catalyst layer morphology was not constant) and therefore it was difficult to design an experiment where catalyst layer morphology and ionomer content (thin film effect) could be investigated independent of one another or exclusively. In other words, an experiment where the catalyst layer morphology is held constant, while ionomer content changes with the goal of exploring the impact of transport resistances on fuel cell performance absent of changes in the catalyst layer morphology at low Pt catalyst loadings.

Other studies have investigated alternative catalyst layer deposition techniques, such as pulse electrodeposition [49], magnetron sputter deposition [50], electrospraying [51,52], electrospinning [53–55], screen printing [56], and inkjet printing [57]. However, regardless of the deposition technique, changing the ionomer content in the catalyst layer affects not only the amount of ionomer that surrounds the catalyst particles, but also the overall morphology of the catalyst layer. Recently, in our laboratory, a new simultaneous electrospinning and electrospraying (E/E) process, shown in Fig. 2, was developed to produce unique nanofiber-nanoparticle electrodes for PEMFCs that resulted in high power densities at ultra-low Pt loadings [58,59]. The E/E technique allows for fabrication of similar catalyst layer morphology while changing other properties (*e.g.*, ionomer content, fiber

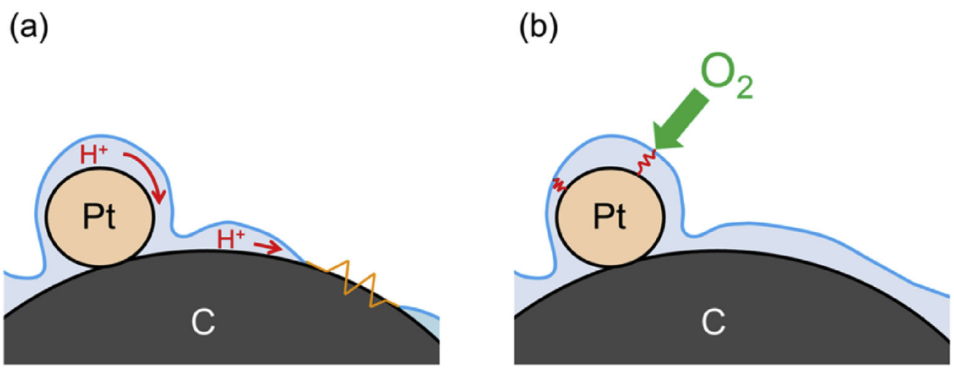

Fig. 1 – Illustration of (a) proton transport resistance due to low Nafion content and (b) mass transport resistance due to Nafion thin film surrounding catalyst particles.

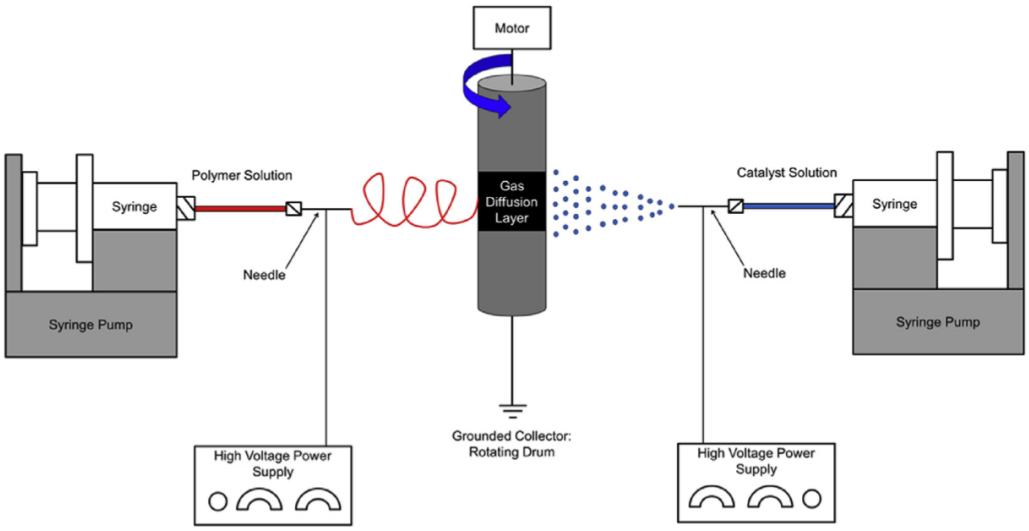

Fig. 2 – Schematic of the electrospinning/electrospraying (E/E) apparatus.

composition, *etc.*), which is difficult to achieve with other catalyst layer deposition techniques, as previously explained. The simultaneous execution of electrospraying and electrospinning increases the number and connectivity of triple phase boundaries by creating a connected network of pores, proton conductive Nafion nanofibers, and electron conductive Pt/C nanoparticles, which differs from conventional electrodes. Here, in this work, E/E electrodes, at various Nafion contents in the electrospraying solution, were fabricated to investigate the impact of Nafion content on catalyst layer transport resistances and fuel cell power density at ultra-low Pt loadings (*ca.* 0.05 mg_{Pt} cm^{-2}). Therefore, this study allows for the exclusive investigation of the effect transport resistances on fuel cell performances at different ionomer contents (thin film effect) at a constant catalyst layer morphology, unlike conventional electrodes.

Experimental

Materials

Isopropanol (IPA; ACS reagent, ≥ 99.5%) and poly(acrylic acid) (PAA; M_V = 450,000 g mol^{-1}) were purchased from Sigma-Aldrich. Carbon (Vulcan XC-72) and 20 wt% platinum on carbon (Pt/C; Vulcan XC-72) were purchased from Premetek Co. 1100 EW Nafion solution (5 wt% in 3/1 v/v isopropanol/water) and Nafion membrane (NR-212, 1100 EW (0.91 meq/g), 0.002 in (~51 μm) dry thickness) were purchased from Ion Power. Gas diffusion layer (GDL; Sigracet 25BC) was purchased from Fuel Cells Etc. All materials were used as received. Deionized (DI) water with a resistivity of 16 MΩ cm was used as appropriate. Ultra-high purity grade nitrogen was purchased from Brazos Valley Welding Supply. Ultra-high purity grade oxygen and ultra-zero grade air were purchased from Airgas. Ultra-high purity grade hydrogen was purchased from Praxair. All gases were used for all fuel cell experiments.

Two-needle electrospinning/electrospraying (E/E) apparatus

A custom-designed E/E apparatus, as illustrated in Fig. 2, consists of two high-voltage power supplies (PS/EL50R00.8, Glassman High Voltage, Inc. and ES40P-10W/DAM, Gamma High Voltage Research, Inc.), two syringe pumps (NE-1000, New Era Pump Systems), two glass syringes (Pt. No. CG-3070-03, Chemglass Life Sciences), two syringe needles (i.d. = 0.024 in. (0.603 mm), Hamilton), poly(vinyl chloride) tubing (Pt. No. 30600-65 and 30600-66, Cole-Parmer), and a grounded collector (cylindrical drum covered with aluminum foil, o.d. = 4.85 cm) connected to a motor (4IK25 GN-SW2, Oriental Motor) to rotate the drum at 135 rpm during the E/E process. Four GDLs (*ca.* 2 cm × 2 cm) were adhered to the drum, where catalyst nanoparticles and polymer nanofibers were electrosprayed and electrospun simultaneously onto the GDLs *via* the E/E process. The needle tip to collector distances, applied voltages, and solution flow rates were 15 and 9 cm, 10 and 12 kV, and 0.3 and 3.3 mL h^{-1} for the electrospinning and electrospraying processes, respectively.

Electrode and membrane electrode assembly (MEA) fabrication

The electrospraying catalyst ink solution used to fabricate E/E electrodes consisted of a base mixture of 20 mg of Pt/C catalyst, ~1–2 mg of bare carbon, 250 mg of DI water, Nafion solution and isopropanol. The particle sizes can vary due to the solids weight percent of the electrospraying solution, thus the solids weight percent was kept constant at 1 wt% for all E/E experiments by adjusting the amount of isopropanol in the mixture. The amount of Nafion solution was adjusted to achieve different amounts of Nafion content of the solids in the electrospraying ink solution as detailed in Table 1. The resulting mixture was sonicated for 3 min at 35% amplitude (Q125, Qsonica) prior to electrospraying. The electrospinning polymer solution used to fabricate E/E electrodes was a 5 wt% 4/1 Nafion/PAA polymer solution, *e.g.*, 25 mg of PAA, 2000 mg

Table 1 – Nafion content of the solids in 1 wt% electrospraying solution.

Nafion content in solids (wt %)	Nafion solution (mg)	Isopropanol (mg)
0	0	1857
19	101	2338
32	200	2704
48	395	3425
65	805	5043
79	1601	8222

of Nafion solution, and 485 mg of 3/1 v/v isopropanol/water solution. The solution was stirred under ambient temperature for at least 12 h to ensure complete dissolution of PAA prior to electrospinning. The catalyst ink solution and the polymer solution were used in the electrospraying and electrospinning processes, respectively, to fabricate E/E electrodes as described in the previous section, and the Pt loading was controlled by the duration of the E/E process. Conventional (control) electrodes were prepared by mixing 100 mg of Pt/C catalyst, 550 mg of DI water, 1000 mg of Nafion solution, and 1350 mg of isopropanol, which corresponds to 2/1 w/w (Pt/C)/Nafion in 3/1 v/v isopropanol/water. The mixture was sonicated for 3 min at 35% amplitude and subsequently brushed onto the GDL with an ox hair brush (0689-00025, Gordon Brush Mfg. Co., Inc.). This process was repeated to achieve the target Pt loading of 0.1 mg_{Pt} cm^{-2}. Membrane electrode assemblies (MEAs) were fabricated by placing the Nafion NR-212 membrane in between two catalyst-coated GDLs (anode and cathode) and heat pressing (3851-0, Carver) for 5 min at 275 °F (135 °C) and 3200 psi (22 MPa). Two MEAs with six different Nafion contents were fabricated for a total of twelve E/E MEAs in this study.

Electrode characterization

The morphology of the E/E electrodes were investigated with scanning electron microscopy (SEM; FEI Quanta 600 FE-SEM, 10 kV for X 5000 magnifications images and 20 kV X 100000 magnification images) using a working distance of 10 mm. Samples were sputter coated (Cressington 208 HR) with platinum/palladium (6 nm thickness) prior to SEM analysis. For each image, the diameters of 20 nanofibers and 20 nanoparticles were randomly selected and measured using ImageJ software for each electrode sample.

The Pt loading was measured with thermal gravimetric analysis (TGA; Q50, TA Instrument). A small portion of the electrode (*ca.* 4–6 mg) was heated in the TGA from ambient temperature to 900 °C at 10 °C min^{-1} in air at 60 mL min^{-1}. Since all components in the E/E electrode degrade below 800 °C with the exception of Pt, the Pt loading was determined by dividing the residual weight at 850 °C by the original area of the TGA sample. The average Pt loading for each E/E experiment was determined using 2–4 samples.

Fuel cell tests and cyclic voltammetry (CV)

Each MEA (1.21 cm^2 area) was placed between two serpentine flow field graphite plates (1 cm^2 flow area) separated by two 0.152 mm thick PTFE/fiberglass gaskets (Cat. No. 33, Scribner Associates, Inc.). The entire fuel cell assembly consisted of an MEA, two gaskets, and two flow plates placed between copper current collectors followed by endplates all held together by bolts with 100 lb in (11.3 N m) of applied torque. Fuel cell performance of each MEA was evaluated with a fuel cell test station (850C, Scribner Associates, Inc.). Fuel cell tests were conducted under ambient pressure with saturated (100% RH) anode and cathode flow rates of 0.43 L min^{-1} hydrogen and 1.02 L min^{-1} oxygen or air, respectively. The stoichiometry of the anode and cathode flow rates used for the fuel cell testing is approximately 1:2 for hydrogen/oxygen and 1:2 for hydrogen/air. The cathode gas, anode gas, and cell temperatures were all maintained at 80 °C. Fuel cell performance was recorded after a new MEA was fully activated. The activation process consists of operating the MEA at 0.7 V for 1 h, followed by 0.6 V, 0.4 V, and 0.2 V for 30 min at each voltage, and ending with two cycles of 0.6 V and 0.4 V for 30 min at each voltage. Polarization curves (cell voltage versus current density) were collected from open circuit voltage (OCV) to 0.2 V at increments of 0.05 V min^{-1} to determine that no further increase in current density at a constant voltage was observed, thus the MEA was at steady state. After the MEA was fully activated and reached steady state, five polarization curves were taken to determine the average maximum power density. The average error between polarization curves was <3% and <5% for the hydrogen/oxygen and hydrogen/air experiments, respectively.

Cyclic voltammetry (CV) was performed on a fully activated MEA with a potentiostat (Solartron SI 1287A, Corrware Software) at 20 mV s^{-1} from 0.01 V to 1 V versus NHE under ambient pressure. In this two-electrode configuration, the anode serves as both the counter and reference electrodes. The fuel cell anode and cathode were supplied with 0.04 L min^{-1} hydrogen and 0.02 L min^{-1} nitrogen, respectively. Temperatures of the cathode gas, anode gas, and cell were maintained at 30 °C. The Pt catalyst was assumed to have an average site density of 210 μC cm^{-2} [60]. The electrochemical surface area (ECSA) was determined from the hydrogen adsorption area from 0.12 to 0.30 V of the CV data. Five cycles were taken to determine the average ECSA for each MEA. Linear sweep voltammetry was performed at 2 mV s^{-1} from OCV to 0.8 V versus NHE to determine if the MEA had any defects that resulted from internal shorts or significant hydrogen crossover.

Electrochemical impedance spectroscopy

Electrochemical impedance spectroscopy (EIS; Solartron SI 1260A) was performed on a fully activated MEA from 1 MHz to 1 Hz at −0.4 V versus OCV (*ca.* 0.49–0.55 V versus NHE) under ambient pressure. In this two-electrode configuration, the anode serves as both the counter and reference electrodes. The fuel cell anode and cathode were supplied with 0.43 L min^{-1} hydrogen and 1.02 L min^{-1} oxygen, respectively. Temperatures of the cathode gas, anode gas, and cell were all maintained at 80 °C. The EIS data was analyzed using a common equivalent circuit model that consisted of a resistor (resistance of the solid electrolyte membrane) in series with a parallel circuit of a constant phase element and a second

resistor (resistance of the catalyst layer) that is typically used to describe a porous electrode [61]. The catalyst layer resistance values reported here are the polarization resistances.

Results and discussion

Fuel cell experiments with E/E catalyst layer electrodes with different Nafion contents (Table 1) were conducted to investigate the effect of the Nafion content on catalyst layer resistances and subsequently on fuel cell performance at a fixed catalyst layer morphology. SEM images of the E/E catalyst layers are shown in Fig. 3(a–f), where each image corresponds to different amounts of Nafion (wt% solids) in the electrospraying solution. The E/E catalyst layers show a highly porous network of randomly arranged nanofibers and particle aggregates, which promotes facile gas transport to Pt sites for reactions to occur. The particle-fiber-pore junction points (*i.e.*, triple phase boundary points) also provide intimate interactions for electron transport, proton transport, and ORR without loss of oxygen gas transport due to the highly porous network as shown in previous studies [58,59]. Fig. 4 shows the average fiber diameters and particle diameters of the images shown in Fig. 3(a–f). The average fiber diameters range from 137 ± 48 nm to 183 ± 64 nm and the average particle diameters range from 1.27 ± 0.71 μm to 1.59 ± 1.34 μm, indicating that the

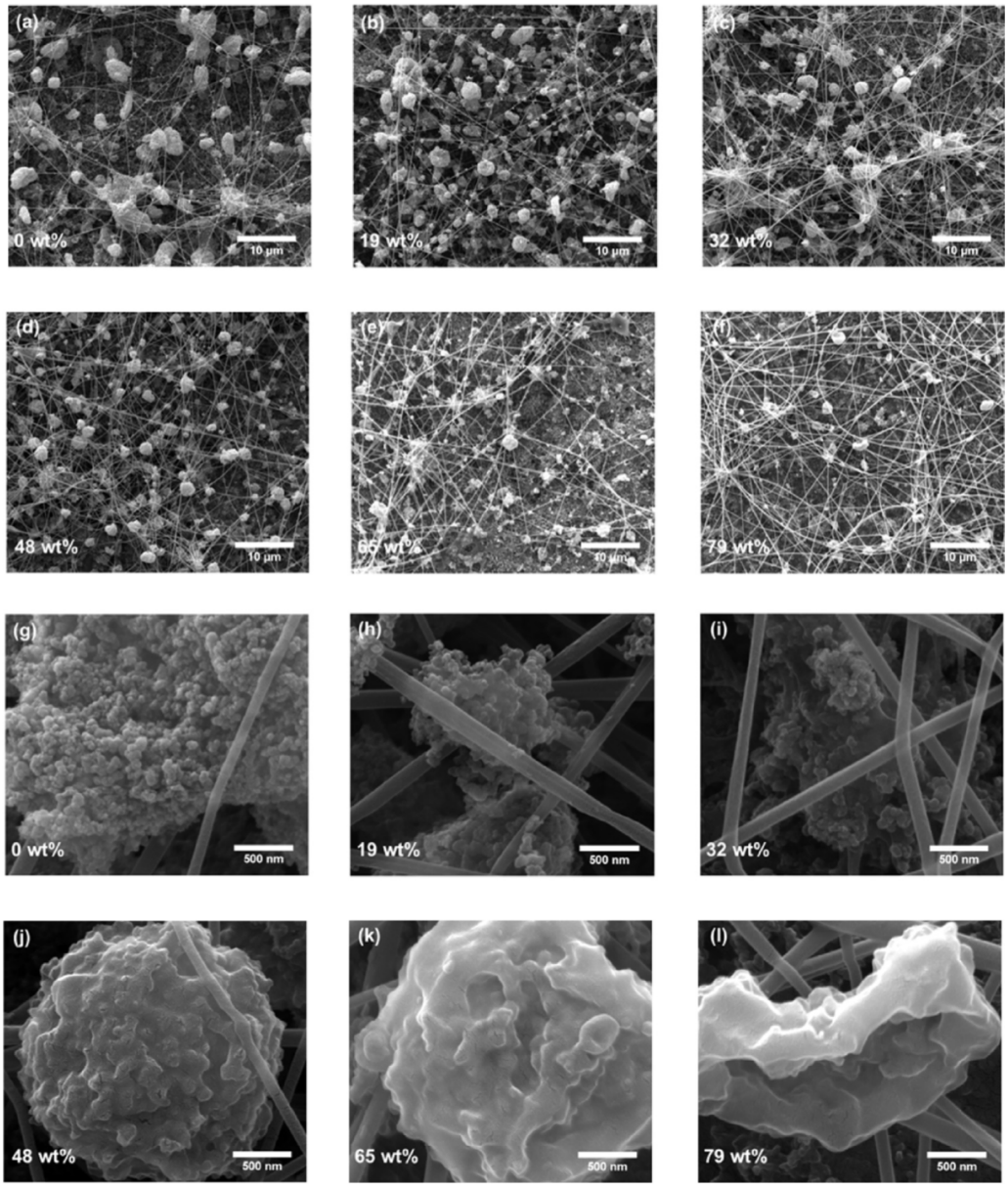

Fig. 3 – SEM images of E/E electrode with various Nafion contents in electrospraying solution: (a,g) 0 wt%, (b,h) 19 wt%, (c,i) 32 wt%, (d,j) 48 wt%, (e,k) 65 wt%, and (f,l) 79 wt%. (a–f) X 5000 magnification, scale bar = 10 μm; (g–l) X 30000 magnification, scale bar = 500 nm.

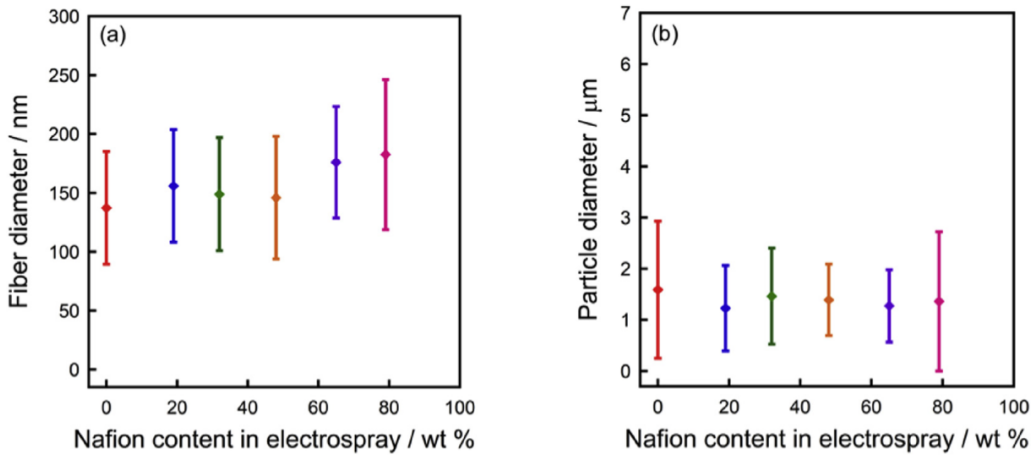

Fig. 4 – (a) Fiber diameters and (b) particle diameters in the E/E catalyst layers as a function of Nafion content in the electrospray.

nanofiber sizes and particle aggregate sizes are similar for all E/E experiments regardless of the amount of Nafion content in the electrospraying solution. The fiber diameter size distributions and particle aggregate size distributions are also similar for all E/E experiments. This result highlights the ability of the E/E process to create catalyst layers with similar overall morphology at different catalyst-to-ionomer ratios or ionomer contents. Thus, the impact of transport resistances due to the ionomer surrounding catalyst particles can be solely investigated without other parameters changing simultaneously.

Fig. 3(g–l) (higher magnification of the catalyst layers; specifically focusing on the catalyst particles) shows that there are distinct visual differences at a local level in the appearance of the particle aggregates at varying amounts of Nafion in the electrospraying solution. From Fig. 3(g)–(i), *i.e.*, from no Nafion to a small amount of Nafion in the electrospraying solution (0–32 wt% Nafion), there is an appearance of polymer that adheres between Pt/C particles. From Fig. 3(j), at 48 wt% Nafion, the Nafion ionomer completely surrounds the particles and creates a thin film around the aggregate. Fig. 3(k) and (l) (65 wt% and 79 wt% Nafion), the Nafion film is thicker and separate Pt/C particles can no longer be distinguished within the aggregates. Therefore, by increasing the amount of Nafion in the electrospraying solution, the particle aggregates begin to change appearance, but maintain relatively similar particle aggregate sizes and overall catalyst layer morphology, while the Nafion ionomer thin film that surrounds the aggregate becomes more visible and thicker. Thus, these results indicate that the amount of Nafion content in the electrospraying solution did not influence the macroscale morphology of the catalyst layer, but influenced the microscale appearance and composition around the catalyst aggregate particles. This allows for the exclusive study of the ionomer resistance on fuel cell performance without altering the overall catalyst layer morphology.

Fig. 5 shows fuel cell performances (polarization and power curves; hydrogen/oxygen and hydrogen/air at ambient pressure at 80 °C) for E/E electrodes at 0.05 mg_{Pt} cm^{-2} total loading (produced with 48 wt% Nafion of the solids in the electrospraying solution) and for conventional painted electrodes (control) at 0.1 mg_{Pt} cm^{-2} total loading. Under hydrogen/

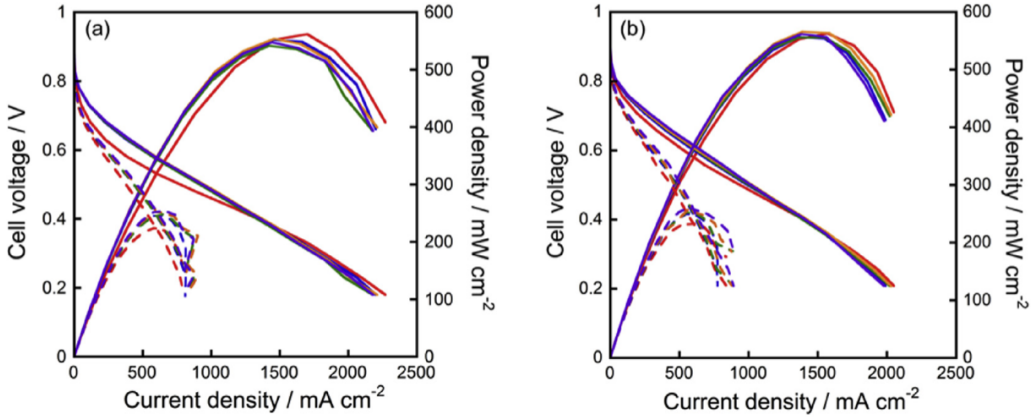

Fig. 5 – Fuel cell performance and polarization curves of MEAs with (a) E/E electrodes with 0.05 mgPt cm^{-2} and (b) conventional electrodes with 0.1 mgPt cm^{-2} under hydrogen/oxygen (solid) and hydrogen/air (dashed).

oxygen, the maximum power density for the E/E electrodes (567 mW cm^{-2}) is similar to that of conventional electrodes (561 mW cm^{-2}) with only 50% of the Pt loading compared to the conventional electrodes. Under hydrogen/air, the maximum power density for the E/E electrodes (262 mW cm^{-2}) is also similar to that of conventional electrodes (250 mW cm^{-2}). These results further emphasize the influence of morphology in ultra-low Pt loading catalyst layers on fuel cell performance as demonstrated in previous studies [58,59].

As shown in Fig. 6(a), the maximum power density for E/E electrodes varies with the amount of Nafion content in the electrospraying ink solution. Under hydrogen/oxygen, from 0 to 32 wt% Nafion content of the solids in the electrospraying solution, there is minimal difference in the maximum power density, which ranges between 415 mW cm^{-2} and 455 mW cm^{-2}. However, at 48 wt% Nafion content of the solids in the electrospraying solution, the power density increases to 567 mW cm^{-2}, which is a 36% gain in power output. From 48 to 65 wt% Nafion content of the solids in the electrospraying solution, the power density slightly decreases to 521 mW cm^{-2}, which corresponds to 8% loss in power output. From 65 wt% to 79 wt% Nafion content of the solids in the electrospraying solution, the power density continues to decrease to 412 mW cm^{-2}, which is an additional 21% loss in power output. This trend is similar for fuel cell performances under hydrogen/air as well. From 0 to 32 wt% Nafion content in the electrospraying solution, there is minimal difference in the maximum power density, which ranges between 170 mW cm^{-2} and 180 mW cm^{-2}. However, at 48 wt% Nafion content of the solids in the electrospraying solution, the power density increases to 262 mW cm^{-2}, which is a 53% gain in power output. From 48 to 65 wt% Nafion content of the solids in the electrospraying solution, the power density decreases to 204 mW cm^{-2}, which corresponds to 22% loss in power output. From 65 wt% to 79 wt% Nafion of the solids in the electrospraying solution, the power density continues to decrease to 142 mW cm^{-2}, which is an additional 30% loss in power output. These results suggest that low Nafion content (0–32 wt% of solids in the electrospraying solution), where the Nafion ionomer has no or little presence as shown in the left inset SEM image in Fig. 6(a), there is no or minimal effect on fuel cell performance; therefore, proton conductivity between the particle aggregates may be constant. This is supported by the SEM images shown previously in Fig. 3(g – i), where the Nafion ionomer does not completely cover the aggregate until 48 wt% as shown in Fig. 3(j). The increase in power density from 32 wt% to 48 wt% Nafion content can be explained by the Nafion ionomer coverage around the particle aggregate which promotes proton conductivity to the triple phase boundaries. As illustrated by Fig. 1(a), the lack of proton pathways will introduce charge transfer resistance, which is evident in the low Nafion content (0–32 wt%) electrodes, where not all of the particle aggregates are visibly connected to the ionomer as shown in the left inset SEM image in Fig. 6(a) (0 wt% Nafion content in the electrospraying solution). However, at 48 wt% Nafion content of the solids in the electrospraying solution, as shown by the middle inset SEM image of Fig. 6(a), there is enough ionomer content that allows each catalyst aggregate to effectively transport protons at each reaction site, as illustrated in Fig. 1(b), which reduces the charge transfer resistance and improves the power density. In addition, the amount of ionomer that surrounds the entire catalyst particle aggregate, as illustrated in Fig. 1(b), is low enough to allow gas to diffuse through, and therefore mass transfer resistance is also minimized. Thus, at 48 wt% Nafion content, the highest maximum power density is achieved by diminishing the charge and mass transfer resistances. At higher Nafion content (65 wt% to 79 wt% of the solids in the electrospraying solution), the power density steadily decreases. As seen previously in Fig. 3(k and l), with higher Nafion content, the

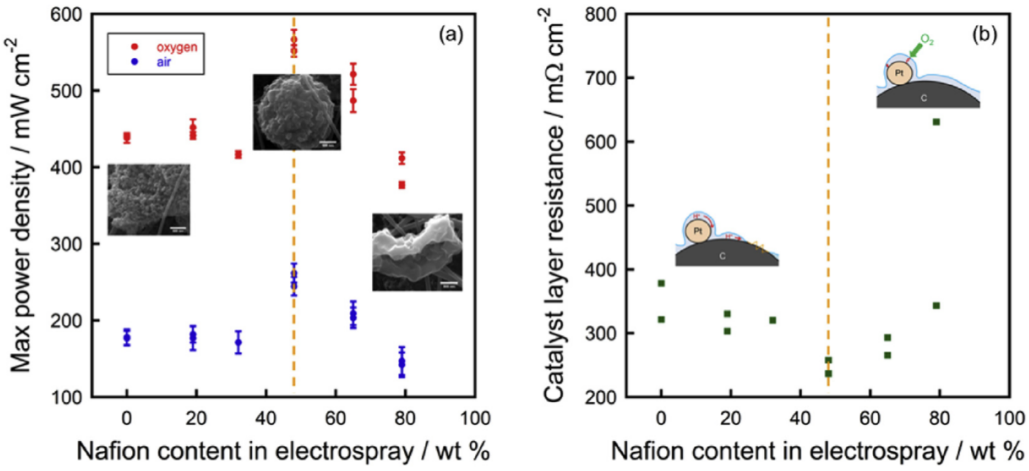

Fig. 6 – (a) Maximum power density under oxygen (red) and air (blue) versus Nafion content in electrospray for E/E MEAs with insets representing high magnification SEM images of catalyst aggregate particles at given Nafion contents: 0 wt%, 48 wt%, and 79 wt% (left to right)) and (b) catalyst layer resistance versus Nafion content in electrospray for E/E MEAs with illustrations of proton transport resistance (left) and mass transport resistance (right). The highest value for maximum power density and minimum resistance is indicated by the dashed vertical line (orange) in (a) and (b), respectively. (For interpretation of the references to colour in this figure legend, the reader is referred to the Web version of this article.)

particle aggregates cannot be visually seen due to the dense ionomer coverage, which increases mass transport resistance. As previously illustrated in Fig. 1(b), mass transport resistance can occur when the solid ionomer blocks reactant gas from reaching Pt reaction sites. This resistance is visually demonstrated by the right inset SEM image in Fig. 6(a) (79 wt% Nafion content of the solids in the electrospraying solution), where the Nafion ionomer completely covers the aggregate and individual particles are no longer distinguishable. Therefore, the solid ionomer becomes a physical barrier for gas diffusion and prevents reactant gas from reaching Pt reaction sites, which effectively decreases the power density.

Electrochemical impedance spectroscopy is a widely used technique to investigate the inner processes of fuel cells, such as electrode degradation [62], proton transfer [63], reaction kinetics on thin film fuel cell electrodes [41], and catalyst layer resistances for PEMFCs [64–66]; specifically ionic conductivities [67–69] and oxygen transport resistances [42]. Springer et al. [64] first proposed and experimentally verified one of the earlier circuit models to describe PEMFCs under operation, and identified and correlated different frequency regimes with different transport processes along the polarization curve. Since then, multiple studies have proposed more complex models to study and identify specific transport processes within the catalyst layer [43,66,69,70]. To further explore the impact of Nafion ionomer on fuel cell performance, the catalyst layer resistance was measured with electrical impedance spectroscopy under hydrogen/oxygen at ambient pressure at 80 °C at −0.4 V versus OCV (*ca.* 0.49–0.55 V versus NHE), which is at a slightly lower voltage compared to the voltage where the maximum power density was observed. As shown in Fig. 6(b), the average catalyst layer resistance is relatively steady between 320 and 350 mΩ cm^2 from 0 to 32 wt% Nafion content of the solids in the electrospraying solution, indicating that at low Nafion content, where proton transport resistance is expected to be high in conventional electrodes due to the poor proton connection between particles and ionomer (as shown in Fig. 3(h) and illustrated in the left inset in Fig. 6(b)), there is little to no effect on fuel cell performance for E/E electrodes because protons can be transferred through the Nafion in the nanofibers, regardless of the amount of Nafion ionomer in the electrospraying solution. From 32 wt% to 48 wt% Nafion content of the solids in the electrospraying solution, there is a decrease in the average catalyst layer resistance from 320 to 240 mΩ cm^2, which suggests that the continuous thin film formation around catalyst particle aggregates (as shown in Fig. 3(k) further improves proton transport and increases the triple phase boundary. From 48 wt% to 79 wt% Nafion content of the solids in the electrospraying solution, the average catalyst layer resistance increases from 240 to 490 mΩ cm^2, which may be attributed to the increase in mass transport resistance as the thin film that surrounds the Pt/C aggregate increases in thickness (as shown in Fig. 3(l) and illustrated in the right inset in Fig. 6(b)). This result suggests that at higher ionomer content in E/E electrodes, mass transport resistance is more dominant than proton transport resistance. Overall, these results show that there is a balance between proton transport and mass transport in E/E electrodes that can be observed by changing the Nafion ionomer content in the electrospray in order to optimize fuel cell performance.

Table 2 summarizes these results: maximum power density, catalyst layer resistance, average electrode Pt loading, and electrochemical surface area (ECSA). The ECSA is a measure of the adsorption or desorption of hydrogen onto the Pt sites; therefore, it is also dependent on the porous structure, electron conductivity, and proton conductivity. From the SEM images, the morphology is similar for all E/E experiments, as stated previously. Therefore, the only difference is the connectivity and thickness of the proton conducting ionomer network surrounding the catalyst particle aggregates, which subsequently depends on the ionomer content in the electrospraying solution. The ECSA steadily increases from 21.9 m^2 g_{Pt}^{-1} to 42.9 m^2 g_{Pt}^{-1} for 0 to 32 wt% Nafion content of the solids in the electrospraying solution, rapidly increases to 99.0 m^2 g_{Pt}^{-1} at 48 wt% Nafion content, and then decreases to 69.6 m^2 g_{Pt}^{-1} and 22.3 m^2 g_{Pt}^{-1} for 65 wt% Nafion content and 79 wt% Nafion content, respectively. The increase in the ECSA may be attributed to the increase in proton transport, which allows for more Pt particles to be accessible, thereby increasing the ECSA. Overall, this trend is similar to the trends observed for power density (Fig. 6(a)) and catalyst layer resistance (Fig. 6(b)). Specifically, at higher Nafion content (from 48 wt% to 79 wt% of solids in the electrospraying solution), the decreasing trend in the ECSA values suggests that the solid ionomer is effectively blocking hydrogen gas from reaching the Pt sites and thereby reducing the amount of available Pt surface area for the reaction to occur.

Table 2 – Pt loading, electrochemical surface area, maximum power density, and catalyst layer resistance for E/E electrodes with different Nafion contents in electrospraying solution.

Nafion content in solids (wt %)	Pt loading (mg_{Pt} cm^{-2})	Max power density[a] (mW cm^{-2})	Max power density[a,c] (kW g_{Pt}^{-1})	Catalyst layer resistance[a] (mΩ cm^2)	ECSA[b] (m^2 g_{Pt}^{-1})
0	0.052	438.2 ± 6.3	4.21 ± 0.06	321.4	21.9 ± 3.1
19	0.041	452.0 ± 10.3	5.51 ± 0.13	303.2	39.2 ± 5.4
32	0.049	416.8 ± 4.3	4.25 ± 0.04	320.4	42.9 ± 5.9
48	0.049	566.8 ± 12.6	5.78 ± 0.13	236.8	99.0 ± 17.2
65	0.042	521.4 ± 13.8	6.21 ± 0.16	265.5	69.6 ± 7.7
79	0.043	411.8 ± 7.6	4.79 ± 0.09	631.0	22.3 ± 2.2

[a] Under H_2/O_2 at 80 °C, ambient pressure.
[b] Under H_2/N_2 at 30 °C, ambient pressure.
[c] Calculated using the total Pt loading in the MEA.

The optimum ionomer content for conventional catalyst layers in fuel cell electrodes has been thoroughly investigated and reported to be approximately 30 wt% [27,29,71]. To compare the optimum total ionomer content in the E/E electrodes to that of conventional electrodes, the total Nafion content in the E/E electrodes, including the Nafion from the nanofibers, was calculated. As shown in Fig. 7, the current density at 0.6 V versus NHE under hydrogen/air for the E/E MEAs from this study is compared to the results from Qi et al. [72] for conventional MEAs. The conventional MEAs show a maximum current density at 30 wt% Nafion content in the electrodes. However, for E/E MEAs, the maximum current density was observed at 62 wt% Nafion, which is a 93% increase from the optimum Nafion content compared to conventional electrodes. Interestingly, one study has shown that the optimum Nafion content changes with Pt loading, and at low Pt loading (0.1 mg_{Pt} cm^{-2}), the optimum Nafion content is 50 wt% [73], which suggests that at ultra-low Pt loadings (<0.1 mg_{Pt} cm^{-2}), the optimum ionomer content may differ from that at a conventional loading (*ca.* 0.4 mg_{Pt} cm^{-2}). Therefore, by utilizing the E/E technique, electrode catalyst layers with ultra-low Pt loadings and different ionomer contents can be investigated to optimize and understand the role of the ionomer thin film resistance on fuel cell performance, while maintaining a constant catalyst layer morphology.

In this study, the fuel cell performance of E/E electrodes were similar to conventional electrodes (control), but the total Pt loading were not similar. Fig. 8 shows fuel cell performance of the E/E electrodes with similar overall Pt loading compared to the control (0.1 mg_{Pt} cm^{-2}). Under hydrogen/oxygen, the

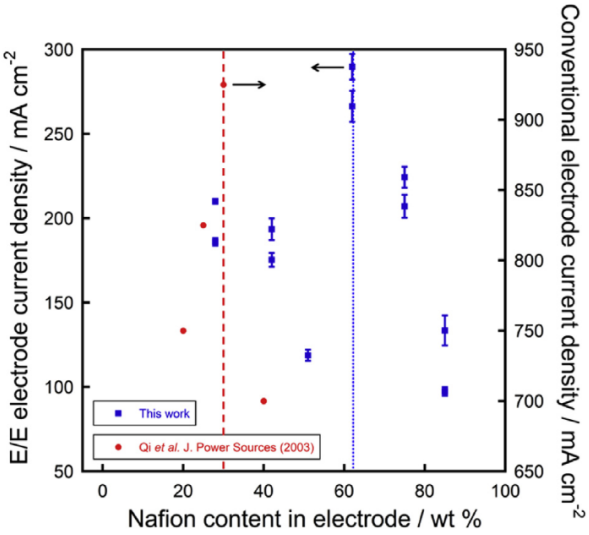

Fig. 7 – E/E electrode current density (blue) and conventional electrode current density (red) versus total Nafion content in the electrode. The optimum total Nafion content is indicated by the dotted (blue) and the dashed (red) vertical lines for the E/E electrode and the conventional electrode, respectively. (For interpretation of the references to colour in this figure legend, the reader is referred to the Web version of this article.)

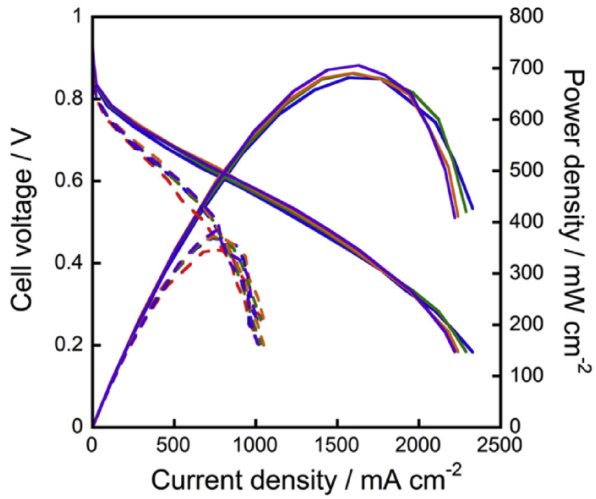

Fig. 8 – Fuel cell performance and polarization curves of MEAs with E/E electrodes with 0.1 mgPt cm^{-2} under hydrogen/oxygen (solid) and hydrogen/air (dashed).

average maximum power density for these E/E electrodes (690 mW cm^{-2}) was observed to be 23% higher than control electrodes (561 mW cm^{-2}) at similar total Pt loadings. Similarly, under hydrogen/air, the average maximum power density for the E/E electrodes (372 mW cm^{-2}) was observed to be 49% higher than that for the control electrodes (250 mW cm^{-2}). Overall, compared to conventional electrodes, the enhanced morphology the E/E electrodes (increased triple phase boundaries) results in similar fuel cell performance at lower Pt loadings or higher fuel cell performance at similar Pt loadings.

Conclusions

In this study, the simultaneous E/E technique provides a platform to produce electrodes with similar overall morphology at various ionomer contents, which allows for the exclusive exploration of the impact of the ionomer thin film on catalyst layer resistances and subsequently fuel cell performances. As ionomer content increased, the catalyst layer resistance decreased and then increased, which was attributed to charge transfer resistance at low ionomer content and mass transport resistance at high ionomer content. However, unlike conventional electrodes, at low ionomer content, a connected proton conducting network still exists in E/E electrodes due to the presence of Nafion nanofibers, and at high ionomer content, a highly porous network still exists in E/E electrodes due to the nanofiber-nanoparticle network. Therefore, the catalyst layer resistances observed are exclusive to the Nafion thin film surrounding the catalyst aggregate particles and not the overall connected pore-ionomer-catalyst morphology. Overall, for E/E electrodes, a maximum in power density and minimum in catalyst layer resistance was observed at 62 wt% Nafion, which differs from conventional electrodes (30 wt%). Furthermore, E/E electrodes had a similar power density compared to conventional electrodes at half

the Pt loading (0.05 mg_{Pt} cm^{-2}) and higher power density at similar Pt loading (0.1 mg_{Pt} cm^{-2}).

Acknowledgements

This work was supported in part by the National Science Foundation under award no. CMMI-1661822. The FE-SEM acquisition was supported by the NSF grant DBI-0116835, the VP for Research Office, and the TX Eng. Exp. Station.

REFERENCES

[1] Kongkanand A, Mathias MF. The priority and challenge of high-power performance of low-platinum proton-exchange membrane fuel cells. J Phys Chem Lett 2016;7:1127–37.
[2] Andreaus B, McEvoy AJ, Scherer GG. Analysis of performance losses in polymer electrolyte fuel cells at high current densities by impedance spectroscopy. Electrochim Acta 2002;47:2223–9.
[3] Gottesfeld S, Zawodzinski TA. Polymer electrolyte fuel cells. Adv Electrochem Sci Eng 1997;5:195–302.
[4] Orfanidi A, Madkikar P, El-Sayed HA, Harzer GS, Kratky T, Gasteiger HA. The key to high performance low Pt loaded electrodes. J Electrochem Soc 2017;164:F418–26.
[5] Sung MT, Chang MH, Ho MH. Investigation of cathode electrocatalysts composed of electrospun Pt nanowires and Pt/C for proton exchange membrane fuel cells. J Power Sources 2014;249:320–6.
[6] Wang F, Yang D, Li B, Zhang H, Hao C, Chang F, Ma J. Investigation of the recoverable degradation of PEM fuel cell operated under drive cycle and different humidities. Int J Hydrogen Energy 2014;39:14441–7.
[7] Wasterlain S, Candusso D, Hissel D, Harel F, Bergman P, Menard P, Anwar M. Study of temperature, air dew point temperature and reactant flow effects on proton exchange membrane fuel cell performances using electrochemical spectroscopy and voltammetry techniques. J Power Sources 2010;195:984–93.
[8] Kim KH, Lee KY, Lee SY, Cho E, Lim TH, Kim HJ, Yoon SP, Kim SH, Lim TW, Jang JH. The effects of relative humidity on the performances of PEMFC MEAs with various Nafion (R) ionomer contents. Int J Hydrogen Energy 2010;35:13104–10.
[9] Pedroza OJO, Dutra JC, Picciani PHS, Dias ML. Morphology and proton conductivity of composite membranes based on poly(styrene sulfonic acid-maleic anhydride) nanofibers prepared by electrospinning. Ionics 2015;21:755–64.
[10] Subramanian C, Giotto M, Weiss RA, Shaw MT. Chemical cross-linking of highly sulfonated polystyrene electrospun fibers. Macromolecules 2012;45:3104–11.
[11] Peng KJ, Lai JY, Liu YL. Nanohybrids of graphene oxide chemically-bonded with Nafion: preparation and application for proton exchange membrane fuel cells. J Membr Sci 2016;514:86–94.
[12] O'Hayre R, Prinz FB. The Air/Platinum/Nafion triple-phase boundary: characteristics, scaling, and implications for fuel cells. J Electrochem Soc 2004;151:A756–62.
[13] Wilson MS, Gottesfeld S. Thin-film catalyst layers for polymer electrolyte fuel-cell electrodes. J Appl Electrochem 1992;22:1–7.
[14] Suzuki T, Kudo K, Morimoto Y. Model for investigation of oxygen transport limitation in a polymer electrolyte fuel cell. J Power Sources 2013;222:379–89.
[15] Afsahi F, Mathieu-Potvin F, Kaliaguine S. Impact of ionomer content on proton exchange membrane fuel cell performance. Fuel Cells 2016;16:107–25.
[16] Wu R, Liao Q, Zhu X, Wang H. Pore network modeling of cathode catalyst layer of proton exchange membrane fuel cell. Int J Hydrogen Energy 2012;37:11255–67.
[17] Xing L, Mamlouk M, Scott K. A two dimensional agglomerate model for a proton exchange membrane fuel cell. Energy 2013;61:196–210.
[18] Moein-Jahromi M, Kermani MJ. Performance prediction of PEM fuel cell cathode catalyst layer using agglomerate model. Int J Hydrogen Energy 2012;37:17954–66.
[19] Suzuki T, Hashizume R, Hayase M. Effect of blending carbon nanoparticles and nanotubes on the formation of porous structure and the performance of proton exchange membrane fuel cell catalyst layers. J Power Sources 2015;286:109–17.
[20] Ahn CY, Hwang W, Lee H, Kim S, Park JE, Kim OH, Her M, Cho YH, Sung YE. Effect of N-doped carbon coatings on the durability of highly loaded platinum and alloy catalysts with different carbon supports for polymer electrolyte membrane fuel cells. Int J Hydrogen Energy 2018;43:10070–81.
[21] Pylypenko S, Borisevich A, More KL, Corpuz AR, Holme T, Dameron AA, Olson TS, Dinh HN, Gennett T, O'Hayre R. Nitrogen: unraveling the secret to stable carbon-supported Pt-alloy electrocatalysts. Energy Environ Sci 2013;6:2957–64.
[22] Jung CY, Yi SC. Improved polarization of mesoporous electrodes of a proton exchange membrane fuel cell using N-methyl-2-pyrrolidinone. Electrochim Acta 2013;113:37–41.
[23] Ngo TT, Yu TL, Lin HL. Influence of the composition of isopropyl alcohol/water mixture solvents in catalyst ink solutions on proton exchange membrane fuel cell performance. J Power Sources 2013;225:293–303.
[24] Kim TH, Yi JY, Jung CY, Jeong E, Yi SC. Solvent effect on the Nafion agglomerate morphology in the catalyst layer of the proton exchange membrane fuel cells. Int J Hydrogen Energy 2017;42:478–85.
[25] Jung C-Y, Kim W-J, Yi S-C. Optimization of catalyst ink composition for the preparation of a membrane electrode assembly in a proton exchange membrane fuel cell using the decal transfer. Int J Hydrogen Energy 2012;37:18446–54.
[26] Gode P, Jaouen F, Lindbergh G, Lundblad A, Sundholm G. Influence of the composition on the structure and electrochemical characteristics of the PEFC cathode. Electrochim Acta 2003;48:4175–87.
[27] Passalacqua E, Lufrano F, Squadrito G, Patti A, Giorgi L. Nafion content in the catalyst layer of polymer electrolyte fuel cells: effects on structure and performance. Electrochim Acta 2001;46:799–805.
[28] Sun CN, More KL, Veith GM, Zawodzinski TA. Composition dependence of the pore structure and water transport of composite catalyst layers for polymer electrolyte fuel cells. J Electrochem Soc 2013;160:F1000–5.
[29] Uchida M, Aoyama Y, Eda N, Ohta A. Investigation of the microstructure in the catalyst layer and effects of both perfluorosulfonate ionomer and PTFE-Loaded carbon on the catalyst layer of polymer electrolyte fuel cells. J Electrochem Soc 1995;142:4143–9.
[30] Lee SJ, Mukerjee S, McBreen J, Rho YW, Kho YT, Lee TH. Effects of Nafion impregnation on performances of PEMFC electrodes. Electrochim Acta 1998;43:3693–701.
[31] Suzuki T, Tsushima S, Hirai S. Effects of Nafion® ionomer and carbon particles on structure formation in a proton-exchange membrane fuel cell catalyst layer fabricated by the decal-transfer method. Int J Hydrogen Energy 2011;36:12361–9.
[32] Lee MR, Lee HY, Yim SD, Kim CS, Shul YG, Kucernak A, Shin D. Effects of ionomer carbon ratio and ionomer

dispersity on the performance and durability of MEAs. Fuel Cells 2018;18:129–36.
[33] Davis EM, Stafford CM, Page KA. Elucidating water transport mechanisms in nafion thin films. ACS Macro Lett 2014;3:1029–35.
[34] Kongkanand A. Interfacial water transport measurements in nafion thin films using a quartz-crystal microbalance. J Phys Chem C 2011;115:11318–25.
[35] Singh RK, Devivaraprasad R, Kar T, Chakraborty A, Neergat M. Electrochemical impedance spectroscopy of oxygen reduction reaction (ORR) in a rotating disk electrode configuration: effect of ionomer content and carbon-support. J Electrochem Soc 2015;162:F489–98.
[36] Shinozaki K, Zack JW, Pylypenko S, Pivovar BS, Kocha SS. Oxygen reduction reaction measurements on platinum electrocatalysts utilizing rotating disk electrode technique II. Influence of ink formulation, catalyst layer uniformity and thickness. J Electrochem Soc 2015;162:F1384–96.
[37] Kudo K, Jinnouchi R, Morimoto Y. Humidity and temperature dependences of oxygen transport resistance of nafion thin film on platinum electrode. Electrochim Acta 2016;209:682–90.
[38] Ono Y, Nagao Y. Interfacial structure and proton conductivity of nafion at the Pt-deposited surface. Langmuir 2016;32:352–8.
[39] Zhang XY, Ding YH. Thickness-dependent structural and transport behaviors in the platinum-Nafion interface: a molecular dynamics investigation. RSC Adv 2014;4:44214–22.
[40] Lin RB, Shih SM. Effects of mass transfer on kinetics of hydrogen oxidation reaction at Nafion/Pt-black thin-film electrodes. J Taiwan Inst Chem E 2013;44:393–401.
[41] Lin R-B, Shih S-M. Kinetics of hydrogen oxidation reaction on Nafion-coated Pt/C electrodes under high overpotentials. J Chin Inst Chem Eng 2007;38:365–70.
[42] Sambandam S, Parrondo J, Ramani V. Estimation of electrode ionomer oxygen permeability and ionomer-phase oxygen transport resistance in polymer electrolyte fuel cells. Phys Chem Chem Phys 2013;15:14994–5002.
[43] Malevich D, Halliop E, Peppley BA, Pharoah JG, Karan K. Investigation of charge-transfer and mass-transport resistances in PEMFCs with microporous layer using electrochemical impedance spectroscopy. J Electrochem Soc 2009;156:B216–24.
[44] Jinnouchi R, Kudo K, Kitano N, Morimoto Y. Molecular dynamics simulations on o 2 permeation through nafion ionomer on platinum surface. Electrochim Acta 2016;188:767–76.
[45] Moore M, Wardlaw P, Dobson P, Boisvert JJ, Putz A, Spiteri RJ, Secanell M. Understanding the effect of kinetic and mass transport processes in cathode agglomerates. J Electrochem Soc 2014;161:E3125–37.
[46] Weber AZ, Kusoglu A. Unexplained transport resistances for low-loaded fuel-cell catalyst layers. J Mater Chem 2014;2:17207–11.
[47] Owejan JP, Owejan JE, Gu WB. Impact of platinum loading and catalyst layer structure on PEMFC performance. J Electrochem Soc 2013;160:F824–33.
[48] Greszler TA, Caulk D, Sinha P. The impact of platinum loading on oxygen transport resistance. J Electrochem Soc 2012;159:F831–40.
[49] Egetenmeyer A, Radev I, Durneata D, Baumgartner M, Peinecke V, Natter H, Hempelmann R. Pulse electrodeposited cathode catalyst layers for PEM fuel cells. Int J Hydrogen Energy 2017;42:13649–60.
[50] Fofana D, Natarajan SK, Bénard P, Hamelin J. High performance PEM fuel cell with low platinum loading at the cathode using magnetron sputter deposition. ISRN Electrochem 2012:2013.
[51] Martin S, Martinez-Vazquez B, Garcia-Ybarra PL, Castillo JL. Peak utilization of catalyst with ultra-low Pt loaded PEM fuel cell electrodes prepared by the electrospray method. J Power Sources 2013;229:179–84.
[52] Oh JW, Na H, Nahm S, Kim Y, Choi H. Multi-layered membrane electrode assembly fabrication by electro-spraying. Ecs Trans 2013;58:1075–83.
[53] Brodt M, Han T, Dale N, Niangar E, Wycisk R, Pintauro P. Fabrication, in-situ performance, and durability of nanofiber fuel cell electrodes. J Electrochem Soc 2015;162:F84–91.
[54] Brodt M, Wycisk R, Pintauro P, Han T, Dale N, Adjemian K. Nanofiber fuel cell electrodes I. Fabrication and performance with commercial Pt/C catalysts. Ecs Trans 2013;58:381–90.
[55] Si D, Zhang S, Huang J, Wang C, Liu Y, Zhang J. Electrochemical characterization of pre-conditioning process of electrospun nanofiber electrodes in polymer electrolyte fuel cells. Fuel Cells 2018;18:576–85.
[56] Hwang DS, Park CH, Yi SC, Lee YM. Optimal catalyst layer structure of polymer electrolyte membrane fuel cell. Int J Hydrogen Energy 2011;36:9876–85.
[57] Shukla S, Domican K, Karan K, Bhattacharjee S, Secanell M. Analysis of low platinum loading thin polymer electrolyte fuel cell electrodes prepared by inkjet printing. Electrochim Acta 2015;156:289–300.
[58] Wang XH, Richey FW, Wujcik KH, Elabd YA. Ultra-low platinum loadings in polymer electrolyte membrane fuel cell electrodes fabricated via simultaneous electrospinning/electrospraying method. J Power Sources 2014;264:42–8.
[59] Wang XH, Richey FW, Wujcik KH, Ventura R, Mattson K, Elabd YA. Effect of polytetrafluoroethylene on ultra-low platinum loaded electrospun/electrosprayed electrodes in proton exchange membrane fuel cells. Electrochim Acta 2014;139:217–24.
[60] Bett J, Kinoshita K, Routsis K, Stonehart P. A comparison of gas-phase and electrochemical measurements for chemisorbed carbon monoxide and hydrogen on platinum crystallites. J Catal 1973;29:160–8.
[61] Paasch G, Micka K, Gersdorf P. Theory of the electrochemical impedance of macrohomogeneous porous electrodes. Electrochim Acta 1993;38:2653–62.
[62] Sudoh M, Kondoh T, Kamiya N, Ueda T, Okajima K. Impedance analysis of gas-diffusion electrode coated with a thin layer of fluoro ionomer to enhance its stability in oxygen reduction. J Electrochem Soc 2000;147:3739–44.
[63] Paul DK, McCreery R, Karan K. Proton transport property in supported nafion nanothin films by electrochemical impedance spectroscopy. J Electrochem Soc 2014;161:F1395–402.
[64] Springer TE, Zawodzinski TA, Wilson MS, Gottesfeld S. Characterization of polymer electrolyte fuel cells using AC impedance spectroscopy. J Electrochem Soc 1996;143:587–99.
[65] Eikerling M, Kornyshev AA. Electrochemical impedance of the cathode catalyst layer in polymer electrolyte fuel cells. J Electroanal Chem 1999;475:107–23.
[66] Ciureanu M, Roberge R. Electrochemical impedance study of PEM fuel cells. Experimental diagnostics and modeling of air cathodes. J Phys Chem B 2001;105:3531–9.
[67] Guo QZ, Cayetano M, Tsou YM, De Castro ES, White RE. Study of ionic conductivity profiles of the air cathode of a PEMFC by AC impedance spectroscopy. J Electrochem Soc 2003;150:A1440–9.
[68] Saab AP, Garzon FH, Zawodzinski TA. Determination of ionic and electronic resistivities in carbon/polyelectrolyte fuel-cell composite electrodes. J Electrochem Soc 2002;149:A1541–6.

[69] Lefebvre MC, Martin RB, Pickup PG. Characterization of ionic conductivity profiles within proton exchange membrane fuel cell gas diffusion electrodes by impedance spectroscopy. Electrochem Solid State Lett 1999;2:259–61.
[70] Makharia R, Mathias MF, Baker DR. Measurement of catalyst layer electrolyte resistance in PEFCs using electrochemical impedance spectroscopy. J Electrochem Soc 2005;152:A970–7.
[71] Thepkaew J, Therdthianwong A, Therdthianwong S. Key parameters of active layers affecting proton exchange membrane (PEM) fuel cell performance. Energy 2008;33:1794–800.
[72] Qi ZG, Kaufman A. Low Pt loading high performance cathodes for PEM fuel cells. J Power Sources 2003;113:37–43.
[73] Sasikumar G, Ihm JW, Ryu H. Dependence of optimum Nafion content in catalyst layer on platinum loading. J Power Sources 2004;132:11–7.